Charge compensation and structural adaptation to accommodate increased magnetic cation content in multiferroic Aurivillius phases

Jennifer Halpin[1,2], Michael Schmidt[1], Roger W. Whatmore[2,3] and Lynette Keeney[1]

1. Tyndall National Institute, University College Cork, Lee Maltings Complex, Dyke Parade, Cork, Ireland.
2. School of Chemistry, University College Cork, Cork, Ireland.
3. Department of Materials, Faculty of Engineering, Imperial College London, London, SW7 2AZ, United Kingdom.

Abstract

The five-layered (*m* = 5) $Bi_6Ti_{2.99}Fe_{1.46}Mn_{0.55}O_{18}$ Aurivillius material is a rare example of a single-phase room temperature ferroelectric-ferromagnetic multiferroic that could ideally be suited to future energy-efficient memory devices. This study examines the effect of *B*-site substitution with the aim of increasing the proportion of magnetic ions within the structure and consequently increasing the saturation magnetisation. Four series of Aurivillius phase films with a target composition of $Bi_6Ti_xFe_yMn_zO_{18}$ (B6TFMO; x = 2.3 to 3.2, y = 1.2 to 2.0, z = 0.3 to 0.9) were fabricated by chemical solution deposition. Substitution of Ti^{4+} by Fe^{3+} and Mn^{3+} necessitates charge compensation mechanisms and requires accommodation of differing ionic radii. While valence changes of Mn^{3+} to Mn^{4+} can act to compensate charge, XRD and TEM analysis is used here to demonstrate that above a threshold of 8 % nominal Mn^{4+}, the *m* = 5 structure can no longer accommodate the smaller Mn^{4+} ion and it rearranges into a mixed-phase material based on *m* = 5 and six-layered (*m* = 6) inter-growths. Increasing the number of perovskite layers by forming the *m* = 6 structure facilitates the accommodation of additional magnetic cations at a lower average manganese oxidation state (+3.3). This work provides valuable insight into the design and development of versatile multiferroic phases by describing how the *B*-site magnetic cation content can be increased to 54 % in *m* = 6 structures, compared to a solubility limit of 46 % in *m* = 5 structures.

1. Introduction

As developments in technology continue to flourish, our reliance on data is also increasing. Data is critical in all aspects of our daily lives and is a vital element in transport networks, power grids and in hospitals. It was estimated that in 2023 digital data storage stood at 64 zettabytes, roughly doubling every two years (1). Contemporary computer storage technologies use either electric or magnetic polarisation to store information separately in single bit devices, and these will soon struggle to keep-up with the ever-increasing trend in demand for data. Not alone does this pose challenges to how enormous levels of information will be efficiently stored; writing and reading data on devices requires power-hungry currents. Masanet *et al*.(2) pointed-out that in 2018, data centres used 205 TWh of electricity, or ca 1 % of global consumption. Interestingly, this was only a 6 % increase on the 2010 figure, despite a 550 % increase in digital data storage over the same period. This was due to major increases in energy efficiency, and it points-up the importance for the sector of maintaining the trajectory of energy-efficiency improvement in the face of ever-increasing demand. Technologies that simultaneously combine ferroelectric and ferromagnetic properties in information storage can use energy-efficient electric fields for the reading and writing of data and could allow an eight-times increase in data storage capacity per cell relative to simple binary switches(3). No such devices exist however, as the ferroelectric-ferromagnetic multiferroic materials needed for this technology are extremely rare. (For the rest of this paper, the term "multiferroic" will be used as a shorthand for "ferroelectric-ferromagnetic multiferroic".)

The Aurivillius phase materials are a family of multilayer perovskites, general formula: $Bi_2O_2(A_{m-1}B_mO_{3m+1})$, where '*m*' is the number of perovskite-type blocks interleaved between $[Bi_2O_2]^{2+}$ fluorite layers (4,5). The structure (6) provides a versatile framework for the design of multiferroic materials (7). They are well-established ferroelectrics (8) and they can accommodate cations such as Fe, Mn, and Cr at their perovskite *B*-sites, which can contribute to magnetic super-exchange interactions (9–13). Indeed, the manganese and iron-containing $Bi_6Ti_{2.99}Fe_{1.46}Mn_{0.55}O_{18}$ (m = 5) (B6TFMO) Aurivillius phase system is an example of a rarely found single-phase room temperature multiferroic, displaying saturation magnetization (M_S) values of 215 emu/cm^3 and in-plane saturation polarisation (P_s) values of $>$ 26 μC/cm (10,11,14).

For utilisation in technologically competitive device applications, a necessary requirement for multiferroic materials is enhancement of the magnetic properties by means of strongly interacting magnetic moments with long-range ordering. A condition for long-range magnetic order is that percolation (connectivity of magnetic species) must be achieved throughout the material system. When considering nearest-neighbour (NN) interactions only, the minimum threshold of magnetic ions in a 3*D* lattice necessary for magnetic percolation is 31 % for a random distribution of the magnetic ions (15). Next-nearest-neighbour (NNN) magnetic interactions also contribute to magnetic order. However, the calculated magnetic Heisenberg coupling constants of NNN interactions in the four-layered (*m* = 4) $Bi_5Ti_3FeO_{15}$ Aurivillius material demonstrate weaker magnetic coupling constants (J_{NNN} = 1 to 2 meV) compared to the NN interactions (J_{NN} = 40 to 50 meV), which enable stronger magnetic coupling constants (16). For the *m* = 5 $Bi_6Ti_{2.99}Fe_{1.46}Mn_{0.55}O_{18}$ composition (10), the magnetic ion content was 40% of *B*-site cations, thus exceeding the minimum percolation threshold and enabling magnetic order at room temperature. For the B6TFMO composition, the particular magnetic exchange interactions and resulting magnetisation are highly dependent on the cation site order and the preference for magnetic cations to partition to the central perovskite layers of the B6TFMO structure (12,17,18).

Insertion of an increased volume of magnetic ions to augment the magnetic fraction beyond the percolation threshold is a strategy to enhance magnetisation even further by promoting long-range magnetic ordering within the B6TFMO system. However, a limit to the concentration of Fe and Mn that can be accommodated within the Aurivillius phase structure is expected. One limitation is based on differences in cation radii (which, when octahedrally coordinated by oxygen are 0.605 for Ti^{4+} and 0.645 Å for both Fe^{3+} and Mn^{3+} in their high spin states (19)). Note that a high-spin state is favoured for transition metals in Aurivillius phase structures due to structural and electronic factors. These factors include the large size of bismuth leading to weaker ligand fields, distortion of the coordination environment due to neighbouring layers, and incomplete hybridisation of metal *d* orbitals with ligand orbitals. Another limitation is because these cations have a nominal valence of 3+ and are substituted in place of Ti, which has a nominal valence of 4+. Replacement of Ti^{4+} by Mn^{3+}/Fe^{3+} requires charge compensation, for which several mechanisms can be postulated. Charge compensation can occur via oxidation state (o.s.) changes of the Mn or Fe cations (10,20,21).

Another possible mechanism is ionic compensation by the introduction of ionic defects such as oxygen vacancies (21–23). Additionally, if the solubility limit is exceeded, segregation of impurity species or secondary phases at grain boundaries or at surfaces can occur (24–26). The presence of $[Bi_2O_2]^{2+}$ layers in Aurivillius phase compounds is recognised to play an important role in space charge compensation, consequently aiding the reduction of leakage currents and improvement of fatigue resistance characteristics (27, 28).

In this study, we systematically examine the effect of varying the concentrations of the three *B*-site atoms: Ti, Fe and Mn in the B6TFMO system $Bi_6Ti_xFe_yMn_zO_{18}$ (x = 2.3 to 3.2, y = 1.2 to 2.0, z = 0.3 to 0.9). The aim of this study was to determine the solubility limit of magnetic ion inclusion in the *m* = 5 Aurivillius structure. We consider the above charge compensation mechanisms and demonstrate that structural reorganisation is a further option available to the versatile Aurivillius phase structures to accommodate increased magnetic fraction.

2. Experimental procedures

2.1 Synthetic procedures

A chemical solution deposition method was used to fabricate the $Bi_6Ti_xFe_yMn_zO_{18}$ compositions using a procedure similar to that previously reported (10). The precursors $Bi(NO_3)_3.5H_2O$ (reagent grade, 98 %, Sigma-Aldrich) and $Ti(OC_4H_9)_4$ (reagent grade, 97 %, Sigma-Aldrich) were dissolved in lactic acid (ACS reagent, ≥ 85 %, Sigma-Aldrich) at room temperature with constant stirring for approximately one week to form “Solution A”. An excess of 17.5 % bismuth precursor was used to compensate for migration of volatile bismuth at the annealing temperatures used to crystallize the films. $Fe(NO_3)_3.9H_2O$ (ACS reagent, ≥ 98 %, Sigma-Aldrich) and ($Mn(acac)_3$) (99.9+ %, Strem Chemicals, Inc.) were dissolved in acetylacetone (≥ 99.5 % (GC), Sigma-Aldrich) to form “Solution B”. Solution B was added to Solution A and mixed for one hour. This precursor solution was placed dropwise onto a *c*-*m* sapphire wafer and then spin coated at 2000 rpm for 30 seconds. The wafer with deposited film was then pre-annealed at 300 °C for ten minutes to remove the organic solvents and then annealed at 850 °C for one hour in ambient atmosphere and pressure to crystallize the films. The average film thickness, as determined by TEM measurements, was calculated to be 89 nm (standard deviation 33 nm across 265 measurement points). The general formulas of the different Series were as follows; Series 1: $Bi_6Ti_3Fe_{1.6-\alpha}Mn_{0.4+\alpha}O_{18}$ (α = 0, 0.1, 0.2, 0.3 and 0.4),

Series 2: $Bi_6Ti_{3.2-\beta}Fe_{1.5}Mn_{0.3+\beta}O_{18}$ (β = 0, 0.1, 0.2, 0.3, 0.4, 0.5 and 0.6), Series 3: $Bi_6Ti_{3.2-\gamma}Fe_{1.3+\gamma}Mn_{0.5}O_{18}$ (γ = 0, 0.1, 0.2, 0.3, 0.4, 0.5 and 0.6) and Series 4 $Bi_6Ti_xFe_yMn_zO_{18}$ (x = 2.3 to 2.8, y = 1.52 to 2.00, z = 0.68 to 0.75).

2.2 X-ray diffraction characterisation

X-ray diffraction measurements (XRD) were performed using a Philips X'pert PW3719 MPD diffractometer, Cu Kα radiation, 40 kV, 35 mA and 2θ range of 6 ˚ to 40 ˚. The *m* = 5 Aurivillius phase was indexed from calculated XRD patterns generated using VESTA (29) and Crystal Diffract 7 software (Crystal Maker Software Ltd.) using data from García-Guaderrama *et al.* (30). The *m* = 6 phase was indexed from calculated XRD patterns using data from Krzhizhanovskaya *et al.* (31).

2.3 Scanning probe microscopy experiments

Atomic Force Microscopy (AFM) and Piezo Force Microscopy (PFM) measurements were performed using an MFP-3D™ Asylum Research instrument. AFM was conducted in AC mode using Olympus AC240TS probes (Al reflex coated, ~7 nm tip radius, 70 kHz resonant frequency). Electromechanical responses of the films were measured by PFM using an Asylum Research MFP-3D™ AFM in contact mode, equipped with a HVA220 Amplifier for PFM using Single Frequency (drive frequency of 20 kHz) and Dual AC Resonance Tracking Piezoresponse Force Microscopy (DART-PFM; contact resonance drive frequency of ~280 kHz) modes. Olympus AC240TM Electrilevers, Ti/Pt coated silicon cantilevers (Al reflex coated, 70 kHz resonant frequency) were used for PFM imaging. Vertical hysteresis loop measurements were obtained by switching spectroscopy PFM (SS-PFM) using a triangular step waveform (comprised of pulse DC bias voltage (25 to 90 V) and an AC signal (5.5 V)). The waveform was cycled twice at a frequency of 0.3 Hz with 68 AC steps per waveform. The Inverse Optical Lever Sensitivity of the cantilevers was calibrated according to the MFP-3D Procedural Operation 'Manualette', the system inherent background was determined using a non-piezoelectric silicon wafer and the PFM was then calibrated using α-quartz as a reference sample. Ferroelectric lithography was performed using the PFM lithography mode by converting an imported greyscale image into a DC bias map (±50 V to ±90 V). Here, the external DC field is applied vertically to the surface using the PFM probe. When the applied

DC field from the PFM probe is greater than the ferroelectric coercive field of a thin film sample, it can induce ferroelectric polarization reversal. The lithography mode enables vertically 'writing' of single domains, domain arrays, and complex patterns without changing the surface topography. The 'read' operation involves PFM detection of written domains using an AC probing voltage (5.5 V).

2.4 Electron microscopy experiments

Scanning electron microscopy (SEM) was performed on a Zeiss Supra 40 instrument and samples were treated with a 3 to 6 nm thickness gold coating before measurement to prevent charging during imaging. Lamella cross sections of the films were prepared using a FEI DualBeam Helios NanoLab 600i Focused Ion Beam instrument. High resolution transmission electron microscopy (HR-TEM) was performed using a Jeol 2100 transmission electron microscope; 200 kV; double tilt holder. Note that normally ~10 % error should be accounted for when calculating distances from TEM data due to the electron optics of the instrumentation. Composition analysis was conducted using high-resolution scanning transmission electron microscopy (STEM) and energy dispersive x-ray spectroscopy (EDX) equipped with an X-Max 80 detector and AZTecanalysis software (Oxford Instruments, Abingdon, UK).

3. Results and discussion

3.1 Structural investigations of *B*-site substitution within the B6TFMO Aurivillius phases

The concentrations of two of the three types of *B*-site cations are systematically varied within the B6TFMO Series 1, 2 and 3, while the third cation concentration is maintained constant. XRD analysis (**Fig. 1 (a)** to **(c)**) of Series 1, 2 and 3 is overall consistent with an m = 5 Aurivillius phase structure. However, in this section we will examine what factors influence deviations away from this.

For Series 1 ($Bi_6Ti_3Fe_{1.6-\alpha}Mn_{0.4+\alpha}O_{18}$ (α = 0, 0.1, 0.2, 0.3 and 0.4)), the concentrations of Fe and Mn are varied, while Ti concentration remains constant. In other words, the Ti : Mn/Fe stoichiometric ratio of 3 : 2 does not change across Series 1. This was considered isovalent substitution since both Fe and Mn are nominally in the 3+ oxidation state (o.s.) in a neutral

B6TFMO Aurivillius stoichiometry. They also have similar ionic radii as noted above (19), although we acknowledge that the Jahn-Teller effect can tend to elongate $Mn^{3+}O_6$ octahedra (32). XRD plots of sample Series 1 are shown **Fig. 1(a)**. The peak positions, heights and widths correlate well with a computed XRD diffraction pattern for a reference *m* = 5 structure (30) shown in Supplementary Information Section **SI1, Fig. SI1**. The reference pattern is computed with an assumed 90 % preferred crystallite (00*l*) orientation, a crystal size of 40 nm and an isotropic strain of 0.75 % to give a line breadth similar to that observed in the *m* = 5 phase in **Fig. 1**, as judged by eye. The 40 nm crystallite size is of the same order-of-magnitude as, but somewhat smaller than, the observed crystallite thickness observed in cross section TEM as shown in **Figures 1 (d)** and **(f)**. As the concentration of Mn increases and Fe decreases, there is only a slight shift (~0.4 °) in 2θ peak positions accompanied by peak broadening. For example, the (00$\underline{10}$) peak FWHM is 0.45 ° for α = 0 and is 0.50 ° for α = 0.4 ($Bi_6Ti_3Fe_{1.6-\alpha}Mn_{0.4+\alpha}O_{18}$). This may indicate some structural disorder within the samples, such as the formation of out-of-phase boundary (OPB) defects, which are common to the Aurivillius structures (12,17,33–35).

The Aurivillius phase structure is highly anisotropic, and the films show strongly preferred *c*-axis orientation, as is evidenced by the majority of XRD peaks displaying (00*l*) reflections. TEM images (**Fig. 1 (d)**) of samples from Series 1 confirm the layered *m* = 5 structure and verify the preferential growth of grains in directions normal to the stacking axis (*c*-axis) of the layers. The grains crystallise with plate-like morphology with grain size ranges from 10 nm to 2 µm (**Fig. 1 (e)**). The crystallites overlap one another at grain boundaries (**Fig. 1 (f)**), meaning that thickness variation is observed across the course of the samples.

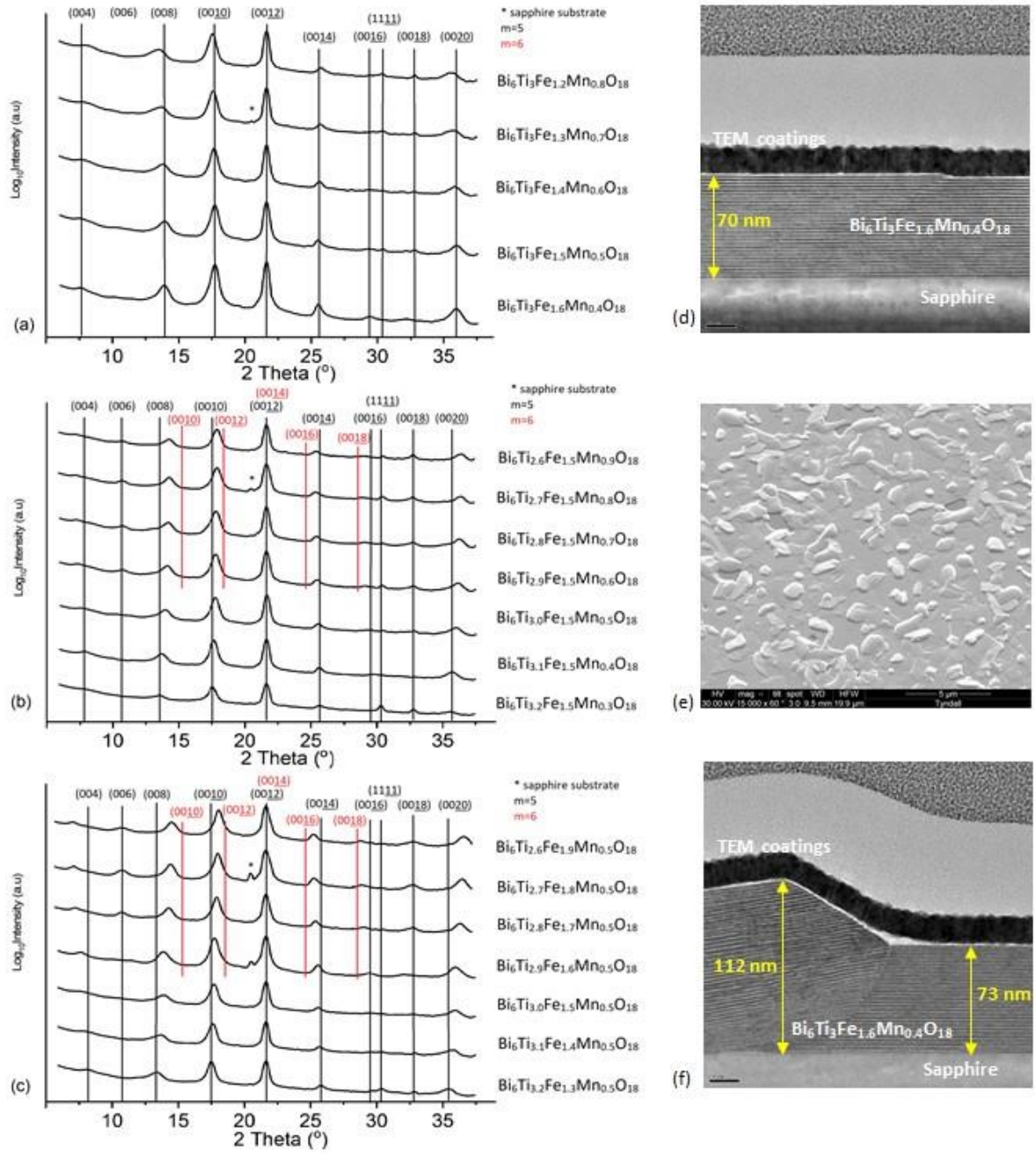

Figure 1. XRD analysis of **(a)** Series 1, **(b)** Series 2 and **(c)** Series 3. **(d)** TEM, **(e)** SEM and **(f)** TEM images of the $Bi_6Ti_3Fe_{1.6}Mn_{0.4}O_{18}$ sample from Series 1 confirm the layered and plate-like Aurivillius phase *m* = 5 structure.

Sapphire substrates were chosen for their cost-effectiveness and because they are chemically stable at the annealing temperatures used to crystallise the Aurivillius phases. However, the sapphire substrate does not possess a simple epitaxial relationship with the Aurivillius material. To determine the mismatch between the Aurivillius phase and the

substrate, the pseudo lattice parameter was calculated using the method given by Newnham and Armstrong (36),

$$a_p = 1.33r_B + 0.6r_A + 2.36\ \text{Å} \qquad \text{(eq. 1)}$$

where r_A is the eight-fold coordinate radius value of the A-site ion (Bi^{3+}) and r_B is the sixfold coordinate radii values of the B-site ions (Ti^{4+}, Mn^{3+} and Fe^{3+}). The pseudo lattice parameter of $Bi_6Ti_3Fe_{1.5}Mn_{0.5}O_{18}$ was calculated to be a_p = 3.85 Å, using radii values reported by Shannon (19). The *a* lattice parameter of the sapphire substrate is 4.78 Å. This yields a 24.2 % lattice mismatch between the substrate and the Aurivillius phase material. This difference is too large to enable a coherent epitaxial relationship between the substrate and the Aurivillius phase film (37). The average film thickness was calculated to be 89 nm, with standard deviation of 33 nm and RMS roughness ranging from 16 to 27 nm. Although Li *et al* (38). reported a slight increase in grain size in Mn-substituted $Bi_5Ti_3Fe_1O_{15}$, possibly due to different thermal dynamic behaviours of Mn and Fe ions (38), in this work, no clear effect on the morphology was observed with the substitution of Fe for Mn. The XRD and TEM data illustrates that isovalent substitution of Mn for Fe in Series 1 does not lead to the significant structural rearrangement to another Aurivillius phase.

Series 2 ($Bi_6Ti_{3.2-\beta}Fe_{1.5}Mn_{0.3+\beta}O_{18}$ (β = 0, 0.1, 0.2, 0.3, 0.4, 0.5 and 0.6)) involves substitution of Ti for Mn and is an example of heterovalent substitution since Ti has a nominal valence of 4+ while the Mn precursor used has a nominal valence of 3+. It is evident from XRD analysis of Series 2 (**Fig. 1 (b)**), that as Ti content decreases and Mn content increases, there is a clear gradual shift in peak position away from the *m* = 5 structure and towards the *m* = 6 Aurivillius phase. For example, as β increases from 0 to 0.6, the 2θ position of the (008) reflection shifts from 13.6 ° to 14.4 ° and the position of the (00$\underline{10}$) reflection shifts from 17.6 ° to 18.0 °. A similar trend in asymmetric peak shift is observed in Series 3 ($Bi_6Ti_{3.2-\gamma}Fe_{1.3+\gamma}Mn_{0.5}O_{18}$ (γ = 0, 0.1, 0.2, 0.3, 0.4, 0.5 and 0.6, **Fig. 1 (c)**), where the *B*-site concentration of Ti is decreased, and the concentration of Fe is increased. For example, as *x* increases from 0 to 0.6, the 2θ position of the (008) reflection moves from 13.4 ° to 14.5 ° and the position of the (00$\underline{10}$) reflection moves from 17.5 ° to 18.1 °.

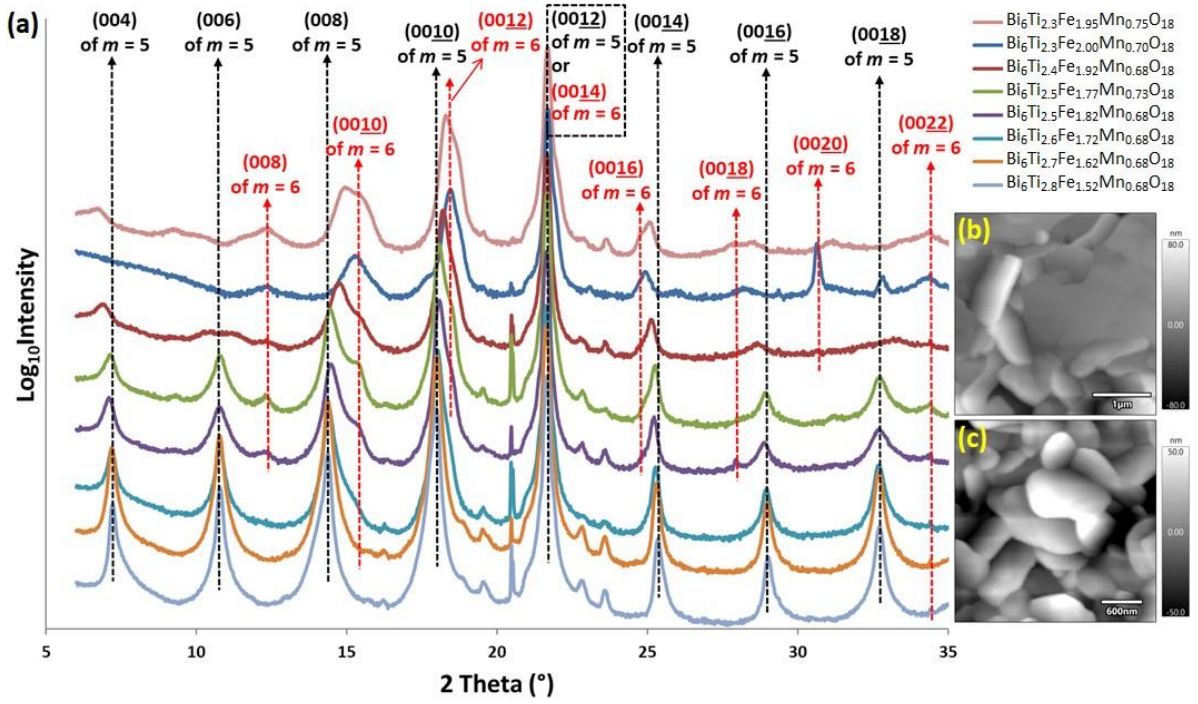

Figure 2. (a) XRD analysis of Series 4. AFM images of the surface morphology for compositions **(b)** $Bi_6Ti_{2.6}Fe_{1.72}Mn_{0.68}O_{18}$ and **(c)** $Bi_6Ti_{2.3}Fe_{1.95}Mn_{0.70}O_{18}$ demonstrate how grains crystallise with plate-like morphology.

The concentration of Ti was further lowered in the samples of Series 4 ($Bi_6Ti_xFe_yMn_zO_{18}$ (x = 2.3 to 2.8, y = 1.52 to 2.00, z = 0.68 to 0.75)). This series involves substitution of Ti by both Mn and Ti (with the concentration of x, y and z allowed to vary over the series) and is another example of heterovalent substitution. XRD data is presented in **Fig. 2 (a)** and AFM images of the surface morphology for compositions $Bi_6Ti_{2.6}Fe_{1.72}Mn_{0.68}O_{18}$ and $Bi_6Ti_{2.3}Fe_{1.95}Mn_{0.70}O_{18}$ are shown in **Fig. 2 (b)** and **(c)**, respectively. As a consequence of a decrease in Ti and an increase in Fe and Mn, the XRD patterns of Series 4 (**Fig. 2 (a)**) clearly show the overall transition away from a pure *m* = 5 sample, to a sample that has a strong *m* = 6 presence. As *x* decreases from 2.8 to 2.3, the (006), (008), (00$\underline{10}$), (00$\underline{14}$), (00$\underline{16}$) and (00$\underline{18}$) reflections of the *m* = 5 structure gradually decrease in peak intensity (e.g. the intensity of the (006) reflection decreases from 38951 counts to 116 counts) and peaks relating to the (008), (00$\underline{10}$), (00$\underline{12}$), (00$\underline{16}$), (00$\underline{18}$) and (00$\underline{20}$) reflections of the *m* = 6 phase begin to emerge, particularly below a Ti concentration of 2.5 at the *B*-site. The XRD patterns resemble the reference plot for a mixed *m* = 5 / *m* = 6 structure, shown in **Fig. SI2**. Note that calculation of *c*-axis lattice parameters

from the XRD data in **Fig. 2 (a)** is complicated by the increased error attributed to the broadening of the peaks as *x* decreases. The full width half maximum (FWHM) values of the XRD peaks increase as the Ti concentration decreases through Series 4 (see Supplementary Information **Section SI2**) and indicates a more disordered periodic structure as *x* decreases. While there is a clear observation for increased formation of the *m* = 6 phase, we learn from TEM analysis presented in **Fig. 3** that regions of *m* = 4 and *m* = 5 also occur in the films. This increased structural stacking disorder within Series 4 results in broadening of the XRD peaks and is reflected in the FWHM values. Contributions to the broadening of the asymmetric peaks may also result from segregation of secondary phases, such as iron or manganese rich perovskites or spinel phases. The presence of secondary phases in particular samples is discussed later (**Section 3.2.3**). Other potential causes of peak broadening could be assigned to particle size effects (39), however the films were deposited using the same deposition method throughout the four series and this consistency should eliminate any significant variation in film thickness and grain size. Accordingly, the observed trend in peak broadening and shift can be attributed to the systematic variation of the stoichiometry.

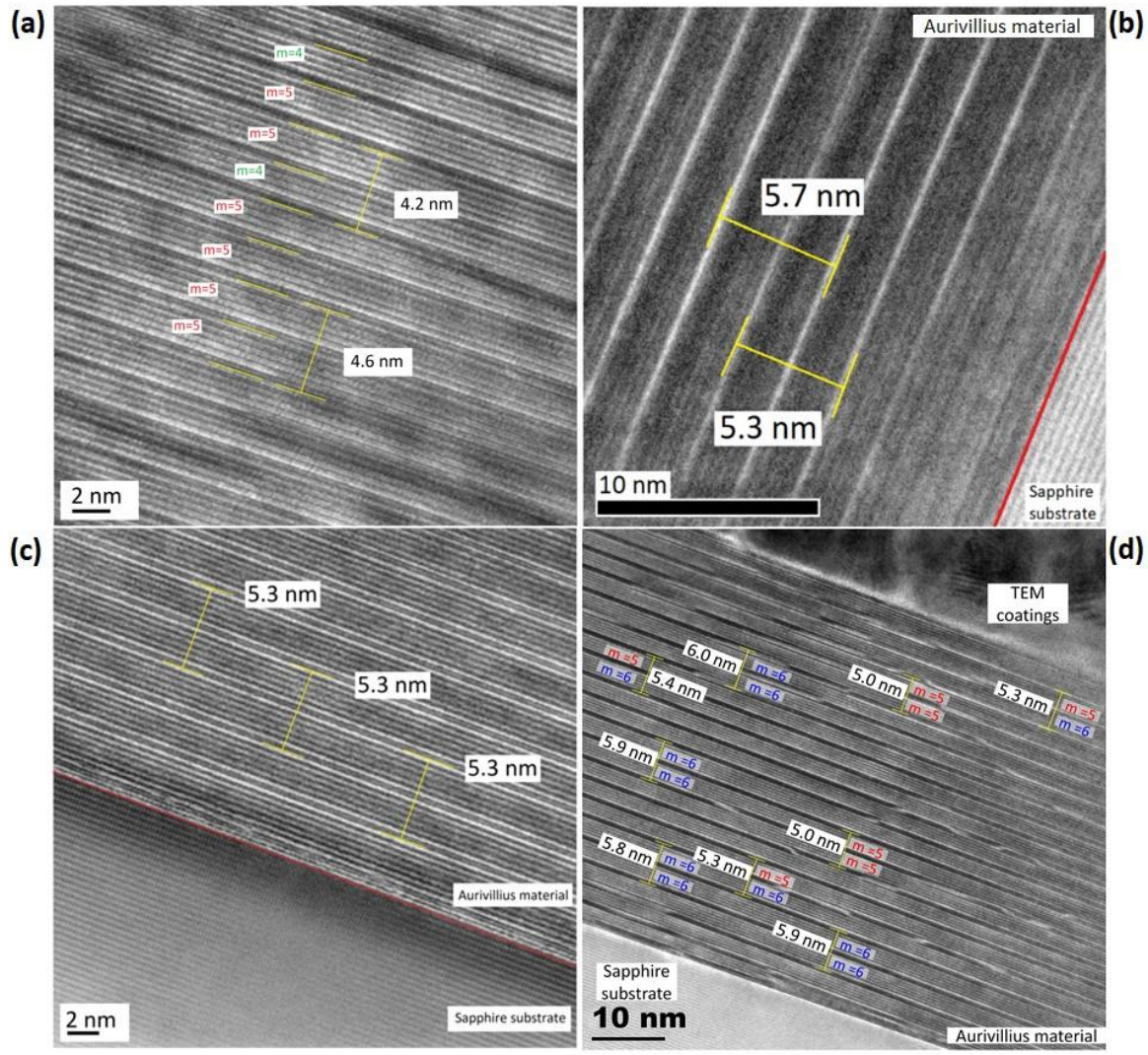

Figure 3. TEM images demonstrating intergrowths of differing Aurivillius phase intergrowths within **(a)** $Bi_6Ti_{2.83}Fe_{1.52}Mn_{0.65}O_{18}$, **(b)** $Bi_6Ti_{2.8}Fe_{1.52}Mn_{0.68}O_{18}$, **(c)** $Bi_6Ti_{2.6}Fe_{1.72}Mn_{0.68}O_{18}$ and **(d)** $Bi_6Ti_{2.3}Fe_{1.95}Mn_{0.75}O_{18}$.

TEM analysis (**Fig. 3**) was used to confirm the increased structural rearrangement to m = 6 layered units as the Ti content within the films decreases. The thickness of a unit cell along the growth (c) axis of the Aurivillius structure can be estimated using the formula

$$c/2 = f + h \qquad \text{(eq. 2)}$$

where $h = m*p.f$ refers to the thickness of the $[Bi_2O_2]^{2+}$ interlayer, which is estimated to be 4.08 Å (40). The average thickness of the perovskite blocks (p) is ≈ 4.11 Å and m refers to the

number of perovskite blocks per half-unit cell of the Aurivillius phase structure (40). Thus, *c* is calculated to be 41.04 Å for an *m* = 4 structure, *c* is 49.26 Å for an *m* = 5 structure and *c* is 57.48 Å for an *m* = 6 structure. This correlates well with the *c*-axis lattice parameters in the literature physically determined by x-ray and powder neutron diffraction data (10,31,41,42). We can then calculate that for a mixed phase sample containing *m* = 5 and *m* = 4 intergrowths, the average *c* value is 45.15 Å. For a mixed phase sample containing *m* = 5 and *m* = 6 intergrowths, the average *c* value is 53.37 Å. Indeed, we observe an increasing presence of mixed *m* = 5 and *m* = 6 phases within the TEM images as the Ti content decreases. TEM data for the $Bi_6Ti_{2.83}Fe_{1.52}Mn_{0.65}O_{18}$ composition in **Fig. 3 (a)** demonstrates the complexity of the films. While most of the sample is *m* = 5 structured (*c*-axis length of 4.6 ± 0.1 nm is within 10 % instrumental error of 4.9 nm), there are still regions of the *m* = 4 Aurivillius phase present. A mixture of *m* = 5 and *m* = 4 units yields a *c*-axis length of 4.2 ± 0.1 nm (within 10 % instrumental error of the expected average *c* value of 4.5 nm). Although XRD data (**Fig. 2 (a)**) demonstrates an overall *m* = 5 structure for the $Bi_6Ti_{2.8}Fe_{1.52}Mn_{0.68}O_{18}$ composition, TEM imaging in **Fig. 3 (b)**, shows that there are local areas within the film displaying unit cell lengths corresponding to intergrowths of *m* = 6 Aurivillius structures (5.7 ± 0.1 nm) and unit cells with a mix of *m* = 5 and *m* = 6 Aurivillius structures (5.3 ± 0.1 nm). Similarly in **Fig. 3 (c)** for the $Bi_6Ti_{2.6}Fe_{1.72}Mn_{0.68}O_{18}$ composition, TEM imaging shows that there are local areas within the film displaying unit cell lengths of 5.3 ± 0.1 nm which infers a mixture of *m* = 5 (~ 4.9 nm) and *m* = 6 (~ 5.7 nm) intergrowths. TEM imaging of the $Bi_6Ti_{2.3}Fe_{1.95}Mn_{0.75}O_{18}$ composition (**Fig. 3 (d)**) confirms the XRD observations (**Fig. 2 (a)**) of a distinct *m* = 6 presence within this sample, accompanied by *m* = 5 intergrowths. The intergrowths of differing *m* phases are often accompanied by OPB defects which can contribute to the peak broadening seen by XRD. The shift to the higher *m*-Aurivillius phase is interesting, given that access to larger layering periods is constrained by thermodynamics. The difference in formation enthalpy between different *m*-phases of similar composition is often too subtle to stabilise one phase relative to another (43), therefore it appears that the chemical modifications are responsible for stabilising the formation of the higher *m*-Aurivillius phase.

3.2 Mechanisms to compensate for charge and size variations during *B*-site substitution

Increasing the concentration of Mn and Fe in this work is motivated by the desire to increase the magnetic ion fraction beyond the percolation threshold and to thereby enhance long-range magnetic ordering within the B6TFMO system. For a $Bi_6Ti_{2.3}Fe_{1.95}Mn_{0.75}O_{18}$ composition, the magnetic ion content would be 54 % of *B*-site cations which is 14 % higher than the $Bi_6Ti_{2.99}Fe_{1.46}Mn_{0.55}O_{18}$ composition which displays an M_S value of 215 emu/cm^3 (11). However, the direct substitution of the lower valence Mn^{3+} and Fe^{3+} for Ti^{4+} results in an unbalanced stoichiometry. Moreover, substitution of Ti^{4+} (0.605 Å) by Fe^{3+} (0.645 Å) and Mn^{3+} (0.645 Å) also involves accommodation of larger ionic radii, which could lead to distortion of the crystal structure. In the following section, we consider possible mechanisms to compensate for charge and size differences when accommodating increased magnetic ion content within the B6TFMO Aurivillius phase system.

3.2.1 Ionic compensation by defects

It is conceivable that the substitution of Ti^{4+} by Fe^{3+} and Mn^{3+} could be accompanied by the formation of compensating oxygen vacancy defects (22,23). However, preliminary density functional theory studies by our group indicate that the formation of oxygen vacancies is energetically unfavourable within the *m* = 5 Aurivillius phases (44). Furthermore, previous work by Snedden *et al.* (24) describes how reports of oxygen deficient Aurivillius phases should be treated with caution. Their work illustrating the difficulty of replacing similarly sized Ti^{4+} by Ga^{3+} in both $Bi_2Sr_2Nb_2TiO_{12}$ (*m* = 3) and $BaBi_4Ti_4O_{15}$ (*m* = 4) indicates the intolerance of the Aurivillius phases (with *m* > 1) towards oxide ion vacancies. McCabe and Greaves (20) also describe the difficulty in formation of an oxygen deficient $Bi_2Sr_2Nb_2MnO_{12-\delta}$ (*m* = 3) Aurivillius phase containing Mn^{3+}. Whereas the synthesis of the $Bi_2Sr_{1.4}La_{0.6}Nb_2MnO_{12}$ (*m* = 3) Aurivillius phase, having a fractional average valency of +3.4 for Mn, in which charge compensation required no oxygen vacancies, was successful. Zurbuchen *et al*. (13) likewise describe that oxide ion vacancies are not favourable for the *m* = 6 Aurivillius phase $Bi_7Mn_{3.75}Ti_{2.25}O_{21}$.

3.2.2 Compensation via oxidation state changes

Assuming that ionic compensation by defects does not play a role, a charge balanced stoichiometry could be achieved on substitution of the lower valence Mn^{3+} and Fe^{3+} for Ti^{4+} through a change in the o.s. of the substituting cations to the 4+ o.s.

Mn is well-established for accommodating variable valency (from three to four) in perovskite oxide materials (45,46). Work by Selbach *et al.* (47,48), on $BiFe_{0.7}Mn_{0.3}O_{3+\delta}$ directly compares the role of manganese and iron in permitting nonstoichiometry to exist. The presence of Mn^{4+}, rather than Fe^{4+}, was utilised to charge compensate the excess oxygen content in their samples. Thermogravimetry was used to determine the nonstoichiometric oxygen content of $\delta = 0.059$ in the manganese containing sample. There was no corresponding excess oxygen ($\delta < 0.01$) in the $BiFeO_{3+\delta}$ sample indicating that Fe^{4+} was not formed during the fabrication process (47,48). The presence of Fe^{4+} has been reported in the domain walls of $BiFeO_3$ samples through detailed HAADF (high-angle annular dark-field) and EELS (electron energy loss spectrum) STEM analysis. However Fe^{4+} accumulates only at the domain wall alongside bismuth vacancies due to differences in the local electrostatic environment; whereas away from the domain walls, Fe^{3+} predominates (21,49). In another study, the substitution of Ni^{2+} for Fe^{3+} in $BiFeO_3$ created a charge imbalance, however this did not result in the formation of Fe^{4+} to compensate. Instead this material favoured the formation of oxygen vacancies, evident from the higher density of free carriers and resulting higher conduction of the Ni substituted materials (50). In general, the oxidation of Fe^{3+} to Fe^{4+} is not common for iron(51) and is not favourable outside of specific conditions, such as near charged domain walls. As such, we expect that an o.s. change mechanism for charge compensation would be facilitated by the oxidation of Mn^{3+} to Mn^{4+} in the Aurivillius phase system.

3.2.3 Segregation of secondary phases

There is also the risk that in response to an increased concentration of iron and manganese, a solubility limit may be surpassed and the segregation of secondary phases such as Fe or Mn-rich perovskites, spinel phases or other oxides may occur (24–26). Given that phases such as Fe_3O_4 and $MnFe_2O_4$ are magnetic in nature, it is obviously important to search for their presence when investigating new compositions as potential multiferroics (14,25,26). No

peaks corresponding to common secondary impurity phases were observed in the XRD analysis of the materials under study in this work. However, it should be noted that the positions of some of these potential impurity peaks may be hidden in XRD analysis due to an overlap with peaks of the Aurivillius material. For example, for the magnetite spinel phase Fe_3O_4, the reflections of the (220) peak at 29.6 ° and the (311) peak at 35.4 ° overlap with the (00<u>16</u>) and (00<u>20</u>) reflection of the Aurivillius *m* = 5 phase, respectively. Additionally, the XRD instrument has a detection limit of approximately 3 vol. %, therefore if secondary phases were present below this volume, they would not be detected (14).

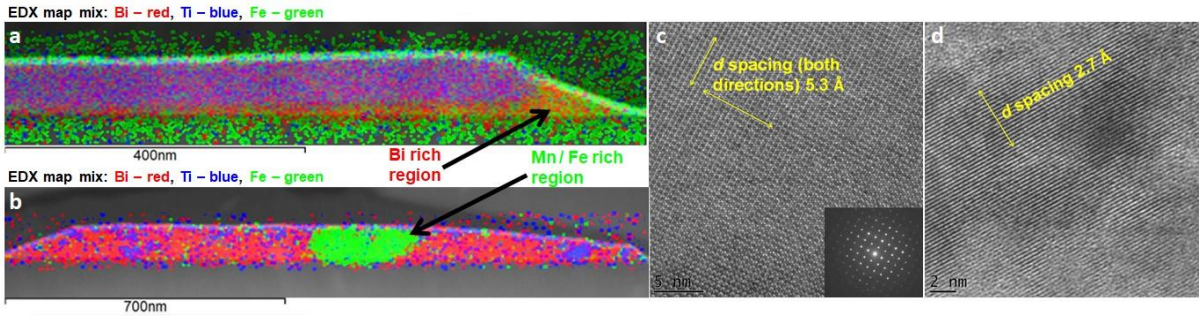

Figure 4. STEM EDX maps of $Bi_6Ti_{2.3}Fe_{1.95}Mn_{0.75}O_{18}$ (46% Ti at the *B*-site) showing the presence of **(a)** bismuth rich and **(b)** manganese/iron-rich regions in the sample at a volume fraction of 2.7 vol. %. **(c)** TEM image and SAED pattern from bismuth and iron-rich cube-shaped crystals. **(d)** TEM image from manganese / iron-rich particles.

In previous work we performed rigorous nano-/micro-structural phase analysis to scrutinise the $Bi_6Ti_{3.0}Fe_{1.5}Mn_{0.5}O_{18}$ (Series 1, 2 and 3) and $Bi_6Ti_{2.8}Fe_{1.52}Mn_{0.68}O_{18}$ (the first member of Series 4 that contained the highest concentration of Ti) samples for possible impurity phases (10,11,14). No impurity phases could be detected and we used the method of statistical inference through the refutation of a null hypothesis to ascertain with a confidence level of ≥99.5 % that the ferromagnetic response in the multiferroic $Bi_6Ti_3Fe_{1.5}Mn_{0.5}O_{18}$ and $Bi_6Ti_{2.8}Fe_{1.52}Mn_{0.68}O_{18}$ compositions was not due to unseen magnetic impurities (10,11,14). In this work, HR-TEM and STEM-EDX analysis was applied by performing a 72-hour EDX map across a 2250 um^2 sample area to investigate the purity of the Aurivillius phase samples containing increased manganese and iron content. Images for

$Bi_6Ti_{2.3}Fe_{1.95}Mn_{0.75}O_{18}$, the last member of Series 4 (containing the lowest concentration of Ti), are shown in **Fig. 4 (a)** to **(d)**. Accompanying the *m* = 6 and *m* = 5 Aurivillius phase structures, which constitute the majority of the sample (refer to **Fig. 3 (c)** and **(d)**), we observe secondary phase impurities adjacent to particular Aurivillius phase crystals and present in the sample at a volume fraction of 2.7 vol. %. One type of impurity detected is an amorphous bismuth rich region (**Fig. 4 (a)**) forming underneath and segregating to the side of individual Aurivillius phase crystals. HR-TEM imaging and STEM-EDX mapping of nearby regions revealed different Fe and Mn rich phases (**Fig. 4 (b)**). We located larger (0.1 to 0.5 μm diameter) bismuth and iron-rich cube-shaped crystals displaying *d*-spacings of 5.3 Å (**Fig. 4 (c)**) (the structure/composition of this secondary phase inclusion could not accurately be determined from the obtained data). Also evident were smaller (< 200 nm) manganese / iron-rich particles with *d*-spacings of 2.7 Å (**Fig. 4 (d)**), which may correspond to the bixbyite $(Mn,Fe)_2O_3$ (cubic Ia-3) phase. It is therefore evident that the $Bi_6Ti_{2.3}Fe_{1.95}Mn_{0.75}O_{18}$ composition has surpassed the limit to the concentration of Fe and Mn that can be accommodated within a phase pure Aurivillius phase structure, and as a result segregation of secondary phases has occurred at a volume fraction of 2.7 vol. %. Previous work on other Aurivillius phase compositions (34,35) has shown that the formation of impurity phases can be reduced by careful control of bismuth excess to counteract its volatility during crystallization. Within the present work, the presence of trace levels of secondary phase impurities would complicate attempts to measure a magnetic signal intrinsic to the main Aurivillius phase (10,11,14,25,26,52), therefore magnetic measurements of the new compositions were not performed in this contribution.

3.2.4 Adaptation by structural rearrangement of the Aurivillius system

From the argument in **Section 3.2.2**, we reason that the decrease in Ti^{4+} is compensated in some part by the oxidation of Mn^{3+} to Mn^{4+}. However, previous work on the Aurivillius phase structures demonstrated the difficulty in forming phase pure structures with substantial amounts of Mn^{4+} on the B-site. For example, McCabe and Greaves (20) reported unsuccessful attempts to prepare $Bi_2Sr_2Nb_2MnO_{12}$ due to the inability to support a significant Mn^{4+} content. Armstrong and Newnham observed that "*substantial substitution*" of *B*-site metals "*is obtained for only a narrow size range of octahedral ions*": 0.58 A° to 0.65 A° (36). It is therefore expected that there will be a limit to how much Mn^{4+} (octahedral site ionic radius 0.53 Å) can

be accepted in the *m* = 5 B6TFMO structure. Along with the precipitation of trace levels of secondary phases (**Section 3.2.3**), XRD analysis (**Fig. 1 and 2**) and TEM imaging (**Fig. 3**) demonstrates that the Aurivillius structure itself is required to adapt to accommodate increased levels of magnetic cations.

Table 1: Proportion of *B*-site ions and calculated Mn(IV) concentrations for differing Aurivillius phase compositions

Composition	Ti *B*-site (%)	Fe *B*-site (%)	Mn *B*-site (%)	% Mn(IV) of Mn	% Mn(IV) overall	Average Mn o.s. in *m* = 5	Average Mn o.s. in *m* = 6	Observed *m* phase
$Bi_6Ti_{3.00}Fe_{1.40}Mn_{0.6}O_{18}$	60.0	28.0	12.0	0.00	0.00	+3.00	+2.17	5
$Bi_6Ti_{3.00}Fe_{1.30}Mn_{0.7}O_{18}$	60.0	26.0	14.0	0.00	0.00	+3.00	+2.29	5
$Bi_6Ti_{2.90}Fe_{1.50}Mn_{0.6}O_{18}$	60.0	30.0	12.0	16.7	2.00	+3.17	+2.33	5
$Bi_6Ti_{2.80}Fe_{1.52}Mn_{0.68}O_{18}$	56.0	30.4	13.6	29.4	3.99	+3.29	+2.56	5
$Bi_6Ti_{2.80}Fe_{1.50}Mn_{0.70}O_{18}$	56.0	30.0	14.0	28.6	4.00	+3.29	+2.57	5
$Bi_6Ti_{2.70}Fe_{1.62}Mn_{0.68}O_{18}$	54.0	32.4	13.6	48.5	6.60	+3.44	+2.71	5
$Bi_6Ti_{2.60}Fe_{1.90}Mn_{0.50}O_{18}$	52.0	38.0	10.0	80.0	8.00	+3.80	+2.80	~5
$Bi_6Ti_{2.60}Fe_{1.72}Mn_{0.68}O_{18}$	52.0	34.4	13.6	58.8	8.00	+3.59	+2.85	~5
$Bi_6Ti_{2.60}Fe_{1.50}Mn_{0.90}O_{18}$	52.0	30.0	18.0	44.4	7.99	+3.44	+2.89	~5
$Bi_6Ti_{2.50}Fe_{1.77}Mn_{0.73}O_{18}$	50.0	35.4	14.6	68.5	10.0	+3.68	+3.00	5 + 6
$Bi_6Ti_{2.50}Fe_{1.82}Mn_{0.68}O_{18}$	50.0	36.4	13.6	73.5	10.0	+3.74	+3.00	5 + 6
$Bi_6Ti_{2.40}Fe_{1.92}Mn_{0.68}O_{18}$	48.0	38.4	13.6	88.2	12.0	+3.88	+3.15	5 + 6
$Bi_6Ti_{2.30}Fe_{2.00}Mn_{0.70}O_{18}$	46.0	40.0	14.0	100	14.0	+4.00	+3.29	6, some 5
$Bi_6Ti_{2.30}Fe_{1.95}Mn_{0.75}O_{18}$	46.0	39.0	15.0	93.3	14.0	+3.93	+3.27	6, some 5

Given that bismuth is used in excess during the synthesis, structural arrangement from an *m* = 5 phase to an *m* = 6 phase is permitted based on the concentrations of cations available. To ascertain the composition where structural adaptation occurs, we tabulate the nominal *B*-site proportion of titanium, iron and manganese for the B6TFMO samples from a spread of compositions with decreasing Ti concentration in **Table 1**. Next, we assume that titanium has a +4 valence, iron has a +3 valence and we let manganese have a valence of either +3 or +4. We then assume that the proportion of Mn^{4+} present is proportional to the concentration necessary to maintain a charge balanced *m* = 5 Aurivillius structure (see Supplementary Information **SI3**). The table is arranged in order of decreasing Ti concentration, and we correlate the compositions with the observations (from XRD and TEM data) of whether the sample shows an overall *m* = 5, *m* = 6 or mixed m = 5/6 Aurivillius phase. **Table 1** demonstrates that the appearance of the *m* = 6 phase (as observed in the XRD and TEM analysis) follows a systematic trend with decreasing Ti concentration. More precisely,

the structural rearrangement occurs when the combined concentration of Fe and Mn at the *B*-site of the perovskite units is above 48 % (see **Table 1**). Furthermore, when the nominal concentration of Mn^{4+} is greater than 8 %, meaning that the average o.s. of Mn in the *m* = 5 structure is larger than ≈ 3.4, the appearance of the *m* = 6 phase begins to occur. We note that this is a similar average o.s. threshold to that previously observed in other Aurivillius phases systems by Zurbuchen *et al.* (13) ($Mn^{3.2+}$) and McCabe and Greaves (20) ($Mn^{3.4+}$).

Given that we have direct evidence from TEM and XRD analysis that evolution of the *m* = 6 phase occurs as the concentration of Ti decreases and Fe and Mn increases, we next consider how structural rearrangement of the Aurivillius phase to higher *m* values enables accommodation of increased Mn content. Scenarios are displayed in **Table 2**. For example, take the chemical composition of the *m* = 5 $Bi_6Ti_{2.30}Fe_{1.95}Mn_{0.75}O_{18}$ composition and rearrange it to the *m* = 6 phase, where it would then assume the $Bi_7Ti_{2.76}Fe_{2.34}Mn_{0.9}O_{21}$ composition. Note that there is a sufficient excess of bismuth included in the chemical solution deposition process to allow for a change in composition and structural rearrangement to an *m* = 6 phase. We note that when we assume an *m* = 5 structural arrangement in **Table 2** (composition $Bi_6Ti_{2.30}Fe_{1.95}Mn_{0.75}O_{18}$), an average manganese o.s. of +3.93 is calculated (assuming oxidation states of +4 and +3 for titanium and iron, respectively). However, when the same ratio of titanium, iron and manganese cations are presented in an *m* = 6 structure (composition $Bi_7Ti_{2.76}Fe_{2.34}Mn_{0.90}O_{21}$), the average manganese o.s. is calculated to be +3.27. The latter is now within the range shown for the stable Aurivillius phase compositions shown by Zurbuchen *et al.* (13)($Mn^{3.2+}$) and McCabe and Greaves (20) ($Mn^{3.4+}$). Here we demonstrate how the formation of the higher *m* = 6 Aurivillius phase would accommodate a higher concentration of magnetic cations while maintaining a balanced stoichiometry. Note that the relative proportions for the *B*-site atoms is the same for both arrangements (**Table 2**), but the proportion of Mn^{4+} needed to achieve a charge balanced stoichiometry is lower for the *m* = 6 phase (3.90 % Mn^{4+} for *m* = 6) compared with the *m* = 5 (13.95 % Mn^{4+}) composition.

Table 2: Examples of stoichiometry/o.s. calculations for *m* = 5 and *m* = 6 Aurivillius phases

	Ti(IV) *B*-Site %	Fe(III) *B*-Site %	Mn *B*-Site %	Mn(IV) % of Mn	Mn(IV)% overall	Mn o.s.	Tolerance factor
$Bi_6Ti_{2.30}Fe_{2.00}Mn_{0.70}O_{18}$ *m*=5	46	40	14	100	14.00	+4.00	0.85

$Bi_7Ti_{2.76}Fe_{2.40}Mn_{0.84}O_{21}$ ***m*=6**	46	40	14	29	4.06	+3.29	0.87
$Bi_6Ti_{2.30}Fe_{1.95}Mn_{0.75}O_{18}$ ***m*=5**	46	39	15	93	13.95	+3.93	0.85
$Bi_7Ti_{2.76}Fe_{2.34}Mn_{0.90}O_{21}$ ***m*=6**	46	39	15	26	3.90	+3.27	0.87

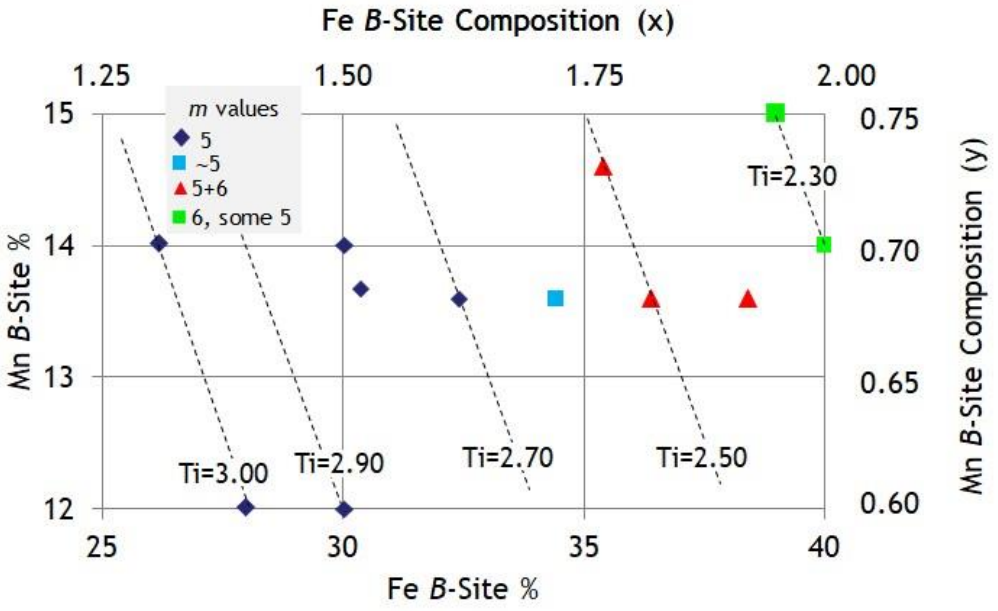

Figure 5. Composition map demonstrating the *m* number for a spread of B6TFMO compositions where the Mn concentration is varied from 0.60 to 0.75.

The inability to accommodate *B*-site concentrations of Mn^{4+} above 8 % in the *m* = 5 structure is the likely driving force behind structural rearrangement and the formation of a higher *m*-Aurivillius phase structure as evident from XRD and TEM analysis. It is also noted that rearrangement to the higher *m*-phase and increased numbers of *A*-site cations increases the tolerance factor (see **Supplementary Information Section SI4**) of the perovskite unit (**Table 2**). The structural adaptation to accommodate increased magnetic cation content in the B6TFMO Aurivillius phases is summarised in the composition map shown in **Fig. 5** (where the Mn concentration varies from 0.60 to 0.75).

This observation of structural reorganisation to an *m* = 6 structure to accommodate increased magnetic fraction in the Aurivillius phases progresses previous studies by Deepak *et al* (53) of tuneable structural changes from an *m* = 3 phase ($Bi_4Ti_3O_{12}$) to an *m* = 4 phase ($Bi_5Ti_3FeO_{15}$) on the addition of iron precursor during chemical vapour deposition growth. The preceding studies revealed that the only way to accommodate an increase in iron and to maintain charge balance between differently charged Fe^{3+} and Ti^{4+} was to accommodate regions of the four-layered Aurivillius structure, accompanied by OPB defects. As the iron concentration was increased further, there was an increase in the random stacking of *m* = 4 layers between *m* = 3 layers and an increase in *c*-axis lattice parameter from 32.274 Å to 40.727 Å. Work by Deepak *et al*. (53) and the current work are examples of charge mediated synthesis, which involves the exploitation of constituents having similar coordination chemistry but different layer charges to impose a particular layer order during crystallisation of a thin film and yield large electronically neutral structural units. In the absence of bulk thermodynamic stability, utilisation of the layer-to-layer charge disparities between the $[Bi_2O_2]^{2+}$ fluorite layers and atomic layers within the perovskite blocks has been shown to stabilise Aurivillius phase homologues with larger values of *m* (e.g. *m* = 7 $Sr_4Bi_4Ti_7O_{24}$) (43), in contrast to Ruddlesden-Popper phases, which possess charge-neutral layers.

3.2.5 Combination of compensation mechanisms

Our study indicates that a combination of charge compensation mechanisms accompanies the increased addition of magnetic cations within the Aurivillius phase thin film samples. Initially oxidation of Mn^{3+} to Mn^{4+} occurs to maintain a balanced stoichiometry when Ti^{4+} is substituted for manganese/iron. However, the substitution of Ti^{4+} by Mn^{4+} is accommodated only up to a certain point before the solubility limit (48 % at the *B*-site) of magnetic cation inclusion in the *m* = 5 Aurivillius structure is reached, and rearrangement of the structure becomes more favourable than oxidation of Mn. The *m* = 5 Aurivillius phase can accommodate up to 7 % Mn^{4+} before rearranging into a mixed-phase material (*m* = 5 and *m* = 6 inter-layers), where the increase in the number of perovskite layers accommodates the increase in Mn content. On increasing the nominal Mn(IV) content to 14 %, the *m* = 5 structure adapts and rearranges to a single phase *m* = 6 structure, where each perovskite block now has 4 % Mn^{4+} on-average. While segregation of impurity phases does not occur for

samples with <44 % magnetic cations at the *B*-site; for samples with nominal 54 % magnetic cations at the *B*-site, the Aurivillius phase composition has surpassed the limit to the concentration of Fe and Mn that can be accommodated within a phase pure Aurivillius phase structure, and as a result segregation of secondary phases occurs (at a volume fraction of 2.7 vol. % in the case of $Bi_6Ti_{2.3}Fe_{1.95}Mn_{0.75}O_{18}$).

3.3 Investigations of ferroelectric properties at the nanoscale as a function of composition and Aurivillius structure

Aurivillius phase materials are established ferroelectrics and polarisation in these materials is predominantly along the *a*-axis, in-plane direction (6,54). We employ lateral piezoresponse force microscopy (PFM) to confirm in-plane piezoelectricity for samples with three different compositions: $Bi_6Ti_{2.80}Fe_{1.52}Mn_{0.68}O_{18}$ (56 % Ti at *B*-site), $Bi_6Ti_{2.50}Fe_{1.77}Mn_{0.73}O_{18}$ (50 % Ti at *B*-site) and $Bi_6Ti_{2.30}Fe_{1.95}Mn_{0.75}O_{18}$ (46 % Ti at *B*-site). The films are naturally self-polarised and the amplitude of the piezoresponse in the lateral direction can be clearly observed in the single frequency (15 kHz) lateral PFM images **Fig. 6 (a)** to **(c).** Regions of uniformly orientated polarity and piezoresponse are represented by polar domains, seperated by domain walls. The substitution of iron and manganese into the structure and the decrease in titanium content does not seem to diminish the in-plane piezoresponse; a clear piezoresponse in the lateral direction is demonstrated for all three compositions. This contrasts with the *m* = 6 $Bi_7Mn_{3.75}Ti_{2.25}O_{21}$ Aurivillius phase composition reported by Zurbuchen *et al* (13). While 62.5 % manganese at the *B*-site enabled ferromagnetic characteristics at 2 K, this was at an expense to the ferroelectric properties, whereupon a reliable ferroelectric response could not be measured for the previously reported $Bi_7Mn_{3.75}Ti_{2.25}O_{21}$ material.

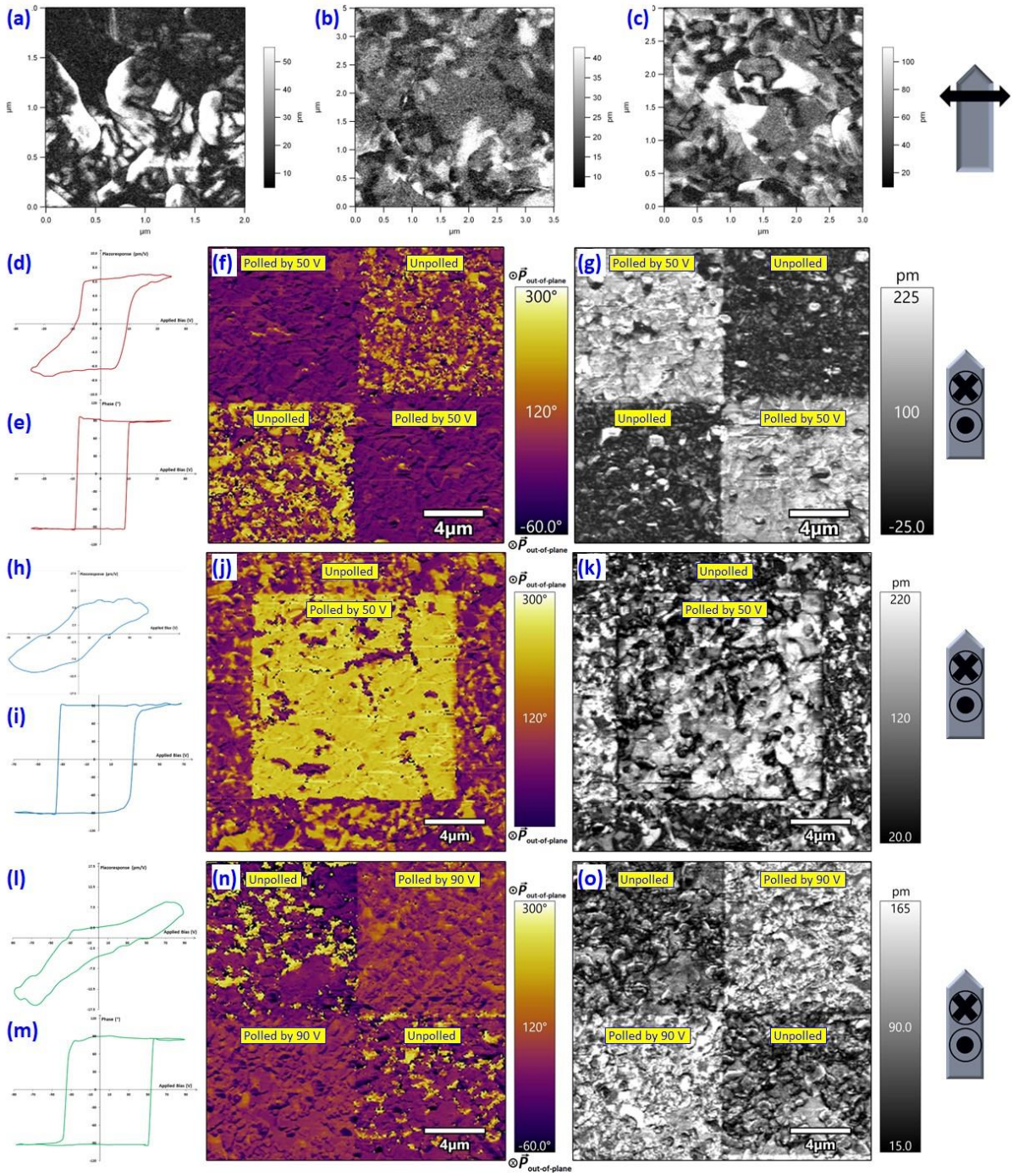

Figure 6. Amplitide images from single frequency PFM measurements in the lateral direction for **(a)** $Bi_6Ti_{2.80}Fe_{1.52}Mn_{0.68}O_{18}$ (56 % Ti at *B*-site), **(b)** $Bi_6Ti_{2.50}Fe_{1.77}Mn_{0.73}O_{18}$ (50 % Ti at *B*-site) and **(c)** $Bi_6Ti_{2.30}Fe_{1.95}Mn_{0.75}O_{18}$ (46 % Ti at *B*-site). Vertical PFM data for $Bi_6Ti_{2.80}Fe_{1.52}Mn_{0.68}O_{18}$: Vertical DART-PFM switching spectroscopy **(d)**, piezoresponse and **(e)** phase loops on removal of an applied DC bias and **(f)** PFM phase image and **(g)** PFM amplitude image after vertical PFM lithography with an applied DC bias of 50 V. Vertical PFM data for $Bi_6Ti_{2.50}Fe_{1.77}Mn_{0.73}O_{18}$: Vertical DART-PFM switching spectroscopy **(h)**, piezoresponse and **(i)** phase loops on removal of an applied DC bias and **(j)** PFM phase image and **(k)** PFM amplitude image after vertical PFM lithography with an applied DC bias of

50 V. Vertical PFM data for $Bi_6Ti_{2.30}Fe_{1.95}Mn_{0.75}O_{18}$: Vertical DART-PFM switching spectroscopy **(l)**, piezoresponse and **(m)** phase loops on removal of an applied DC bias and **(n)** PFM phase image and **(o)** PFM amplitude image after vertical PFM lithography with an applied DC bias of 90 V.

In terms of out-of-plane ferroelectric properties, Aurivillius phases with odd and even numbers of perovskite layers behave differently. Polar Aurivillius phases having even numbers of *m* perovskite layers, such as the *m* = 6 Aurivillius phase, retain a mirror plane perpendicular to the *c*-axis. This prohibits out-of-plane polarisation in even-layered Aurivillius phases and the polarisation is confined to the lateral plane. On the other hand, for Aurivillius phase materials with an odd number of perovskite blocks, retention of the mirror plane is not energetically favourable and a minor polarisation is expected along the *c*-axis out-of-plane direction in conjunction with a major in-plane polarisation (55). A minor polarisation along the *c*-axis is therefore expected in the *m* = 5 Aurivillius phases due to the structure having an odd number of perovskite blocks. However as the samples reorganise to accommodate more of the *m* = 6 plase, we would expect the polarisation response along the out-of-plane *c*-axis direction to decrease.

To examine the local out-of-plane ferroelectric and piezo- response as a function of composition and Aurivillius structure, vertical PFM studies were performed on the samples. Electromechanical switching properties were probed locally by vertical switching spectroscopy PFM (SS-PFM). The phase and amplitude as a function of applied electric field in the vertical direction are shown in the hysteresis loops shown in Fig. 6 (**Fig. 6 (d)** to **(m)**). The local polarization switching response data demonstrates that the phase of domains switches 180° in the vertical direction for all three samples, however the coercive voltage (width of the hysteresis loop) increases to values of 9.0, 30.1, and 41.8 V for $Bi_6Ti_{2.80}Fe_{1.52}Mn_{0.68}O_{18}$ (56 % Ti at *B*-site), $Bi_6Ti_{2.50}Fe_{1.77}Mn_{0.73}O_{18}$ (50 % Ti at *B*-site) and $Bi_6Ti_{2.30}Fe_{1.95}Mn_{0.75}O_{18}$ (46 % Ti at *B*-site) respectively (**Fig. 6 (e)**, **(i)**, **(m)**). The vertical displacement amplitude as a function of applied DC bias for the for $Bi_6Ti_{2.80}Fe_{1.52}Mn_{0.68}O_{18}$ (56 % Ti at *B*-site) and $Bi_6Ti_{2.50}Fe_{1.77}Mn_{0.73}O_{18}$ (50 % Ti at *B*-site) compositions displays a hysteresis loop shape characteristic of ferroelectric materials with piezoresponse values of 6.4 and 7.6 pm/V, respectively (**Fig. 6 (d)**, **(h)**). However, the vertical piezoresponse decreased to 3.6

pm/V for the $Bi_6Ti_{2.50}Fe_{1.77}Mn_{0.73}O_{18}$ (50 % Ti at *B*-site) composition (**Fig. 6 (l)**). Furthermore, hysteresis shape is not concave for the $Bi_6Ti_{2.50}Fe_{1.77}Mn_{0.73}O_{18}$ (50 % Ti at *B*-site) composition, resembling characteristics of a lossy dielectric (56). For the iron-containing $Bi_4Bi_{m-3}Fe_{m-3}Ti_3O_{3m+3}$ phases, it was previously shown that the leakage current increased as m increased from 4 to 6 (57). The presence of non-ferroelectric secondary-phase impurities within the $Bi_6Ti_{2.50}Fe_{1.77}Mn_{0.73}O_{18}$ sample, constituting a volume fraction of 2.7 vol. %, could also be a factor influencing domain wall pinning, reduced polarisation value, increased coercive field and an altered hysteresis loop shape. Ferroelectric lithography investigations (**Fig. 6 (f)**, **(g)**, **(j)**, **(k)**, **(n)**, **(o)**) confirm the trend for the requirement of higher DC fields for vertical domain switching as the *B*-site Ti concentration is lowered and the presence of the *m* = 6 phases increases. Application of a DC bias of 50 V vertically to regions on the BTF7M3O thin films ("write" step), produced ferroelectric polarisation reversal in the $Bi_6Ti_{2.80}Fe_{1.52}Mn_{0.68}O_{18}$ (56 % Ti at *B*-site), $Bi_6Ti_{2.50}Fe_{1.77}Mn_{0.73}O_{18}$ (50 % Ti at *B*-site) films, as detected by the subsequent PFM scan ("read" step) ((**Fig. 6 (f)**, **(g)**, **(j)**, **(k)**). However, a DC bias of 90 V was required for vertical switching of ferroelectric domains in the $Bi_6Ti_{230}Fe_{1.95}Mn_{0.75}O_{18}$ (46 % Ti at *B*-site) sample (**Fig. 6 (n)**, **(o)**).

4. Conclusions

This study contributes a comprehensive understanding of charge and size compensation mechanisms aimed at accommodating higher concentrations of magnetic cations in multiferroic Aurivillius phases. The initial investigation focused on determining the solubility limit for magnetic Fe and Mn cations within the *m* = 5 Aurivillius phase structure. XRD and TEM analyses of $Bi_6Ti_xFe_yMn_zO_{18}$ (x = 2.3 to 3.2, y = 1.2 to 2.0, z = 0.3 to 0.9) compositions revealed that when the Ti^{4+} content was lowered below 52 %, a discernible transformation occurs, leading to the formation of a mixed-phase sample consisting of both the main *m* = 5 Aurivillius phase and the *m* = 6 phase. The prevalence of the *m* = 6 phase within the *m* = 5 phase matrix increased with decreasing Ti^{4+} content. It is postulated that the depletion of Ti^{4+} is initially compensated by the oxidation of Mn^{3+} to Mn^{4+} to maintain overall charge neutrality. The presence of Mn^{4+} has significant implications for the type of magnetic behaviour expected, as the Mn^{3+} - O - Mn^{4+} and Fe^{3+} - O - Mn^{4+} double exchange mechanism promotes ferromagnetic behaviour, contrasting with the superexchange mechanism between Mn^{3+} - O

- Mn^{3+}, which favours antiferromagnetic behaviour (58–60). However, the cation radius disparity restricts the maximum concentration of Mn^{4+} that can be accommodated by the structure. These findings indicate that there exists a threshold Mn^{4+} solubility limit of 8 % (or 48 % magnetic ion content at the *B*-site). Beyond this threshold, the *m* = 5 phase undergoes a transformation, favouring the adoption of the higher *m* = 6 homologue. Upon elevating the nominal Mn(IV) content to 14%, the structure transforms into a single-phase *m* = 6 structure, with each perovskite block now containing 4% Mn(IV). The transition to the higher-layered Aurivillius homologue is interesting, especially considering the thermodynamic constraints on expanding layering periods (43). It suggests that chemical modifications are pivotal in stabilising the formation of the *m* = 6 Aurivillius phase. This transition to the higher *m* = 6 phase reduces the relative fraction of Mn^{4+} required for charge neutrality in the material (refer to **Table 2**). Consequently, the structure becomes more tolerant of higher magnetic cation content. Correspondingly, the average calculated oxidation state for manganese also decreases, falling within the range of values reported previously (13,20) for stable Aurivillius phase compositions.

Moreover, the percolation fraction, which is crucial for long-range magnetic ordering, also increases upon phase transformation. For instance, in the *m* = 6 composition $Bi_7Ti_{2.76}Fe_{2.34}Mn_{0.90}O_{21}$, the magnetic cation content reaches 54% of B-site cations, which is 14% higher than the multiferroic $Bi_6Ti_{2.99}Fe_{1.46}Mn_{0.55}O_{18}$ composition that exhibits an M_S value of 215 emu/cm^3 (11). Notably, the predominant in-plane piezoresponse of these materials is unaffected by magnetic cation substitution. However, as expected from crystal symmetry, the minor out-of-plane ferroelectric response diminishes with increasing structural reorganisation towards the *m* = 6 phase.

This study provides valuable insights into the limiting factors that govern magnetic ion substitution at the *B*-site of Aurivillius materials, which should be considered during the development of new multiferroic materials.

Acknowledgements

The authors gratefully acknowledge the support of Science Foundation Ireland (SFI) Principle Investigator Award Number 15/IA/3015 DEPO-Man, 'Design, Deposition and Exploitation of

Novel Micro and Nano-scale Materials and Devices for Advanced Manufacturing', support of SFI under the FORME Strategic Research Cluster Award number 07/SRC/I1172, support from the SFI Frontiers for the Future Project 19/FFP/6475 and support from the Royal Society and SFI University Fellowships UF 140263 and URF\R\201008. JH and LK thank Professor Martyn Pemble (Emeritus, University College Cork) for his mentorship during the course of this project.

References

1. Bartley K. Big statistics: how much data is there in the world? [Internet]. Big statistics: how much data is there in the world? Available from: https://rivery.io/blog/big-data-statistics-how-much-data-is-there-in-the-world/

2. Masanet E, Shehabi A, Lei N, Smith S, Koomey J. Recalibrating global data center energy-use estimates. Science. 2020;367(6481):984–6.

3. Yang F, Tang MH, Ye Z, Zhou YC, Zheng XJ, Tang JX, et al. Eight logic states of tunneling magnetoelectroresistance in multiferroic tunnel junctions. J Appl Phys. 2007 Aug 22;102(4):044504.

4. Aurivilllius B. Mixed Bismuth Oxides with layer lattices I. The structure type of CaNb2Bi2O9. Ark Kemi. 1949;1(54):463–80.

5. Aurivillius B. Mixed Bismuth Oxides With Layer Lattices. 2. Structure of Bi4Ti3O12. Ark Kemi. 1950;1(6):499–512.

6. Newnham RE, Wolfe RW, Dorrian JF. Structural basis of ferroelectricity in the bismuth titanate family. Mater Res Bull. 1971 Oct 1;6(10):1029–39.

7. Tinte S, Stachiotti MG. Multiferroic behavior of Aurivillius Bi_4Mn_3O_12 from first principles. Phys Rev B. 2012 Jun;85(22):224112.

8. Subbarao EC. Ferroelectricity in \mathrmBi_4\mathrmTi_3\mathrmO_12and Its Solid Solutions. Phys Rev. 1961 May;122(3):804–7.

9. Giddings AT, Stennett MC, Reid DP, McCabe EE, Greaves C, Hyatt NC. Synthesis, structure and characterisation of the n=4 Aurivillius phase Bi5Ti3CrO15. J Solid State Chem. 2011 Feb 1;184(2):252–63.

10. Keeney L, Maity T, Schmidt M, Amann A, Deepak N, Petkov N, et al. Magnetic Field-Induced Ferroelectric Switching in Multiferroic Aurivillius Phase Thin Films at Room Temperature. J Am Ceram Soc. 2013 Aug 1;96(8):2339–57.

11. Faraz A, Maity T, Schmidt M, Deepak N, Roy S, Pemble ME, et al. Direct visualization of magnetic-field-induced magnetoelectric switching in multiferroic aurivillius phase thin films. J Am Ceram Soc. 2017 Mar 1;100(3):975–87.

12. Keeney L, Downing C, Schmidt M, Pemble ME, Nicolosi V, Whatmore RW. Direct atomic scale determination of magnetic ion partition in a room temperature multiferroic material. Sci Rep. 2017 May 11;7(1):1737.

13. Zurbuchen MA, Freitas RS, Wilson MJ, Schiffer P, Roeckerath M, Schubert J, et al. Synthesis and characterization of an n=6 Aurivillius phase incorporating magnetically active manganese, Bi7(Mn,Ti)6O21. Appl Phys Lett. 2007 Jul 20;91(3):033113.

14. Schmidt M, Amann A, Keeney L, Pemble ME, Holmes JD, Petkov N, et al. Absence of Evidence ≠ Evidence of Absence: Statistical Analysis of Inclusions in Multiferroic Thin Films. Sci Rep. 2014 Jul 16;4(1):5712.

15. Kurzawski Ł, Malarz K. Simple Cubic Random-Site Percolation Thresholds for Complex Neighbourhoods. Rep Math Phys. 2012 Oct 1;70(2):163–9.

16. Birenbaum AY, Ederer C. Potentially multiferroic Aurivillius phase \mathrmBi_5\mathrmFeTi_3\mathrmO_15: Cation site preference, electric polarization, and magnetic coupling from first principles. Phys Rev B. 2014 Dec;90(21):214109.

17. Moore K, O'Connell EN, Griffin SM, Downing C, Colfer L, Schmidt M, et al. Charged Domain Wall and Polar Vortex Topologies in a Room-Temperature Magnetoelectric Multiferroic Thin Film. ACS Appl Mater Interfaces. 2022 Feb 2;14(4):5525–36.

18. Colfer L, Bagues N, Noor-A-Alam M, Schmidt M, Nolan M, McComb D, et al. Atomic level origin of the impact of octahedral tilting and tetragonal distortions on the functional properties of the room temperature multiferroic Bi6Ti3Fe1.5Mn0.5O18. ChemRxiv: ChemRxiv; 2024.

19. Shannon RD. Revised effective ionic radii and systematic studies of interatomic distances in halides and chalcogenides. Acta Crystallogr Sect A. 1976 Sep 1;32(5):751–67.

20. McCabe EE, Greaves C. Structural and magnetic characterisation of Bi2Sr1.4La0.6Nb2MnO12 and its relationship to "Bi2Sr2Nb2MnO12". J Mater Chem. 2005;15(1):177–82.

21. Rojac T, Bencan A, Drazic G, Sakamoto N, Ursic H, Jancar B, et al. Domain-wall conduction in ferroelectric BiFeO3 controlled by accumulation of charged defects. Nat Mater. 2017 Mar 1;16(3):322–7.

22. Gradauskaite E, Hunnestad KA, Meier QN, Meier D, Trassin M. Ferroelectric Domain Engineering Using Structural Defect Ordering. Chem Mater. 2022 Jul 26;34(14):6468–75.

23. Patri T, Ghosh A, Mahesh MLV, Babu PD, Mandal SK, Singh MN. Fortified relaxor ferroelectricity of rare earth substituted 4-layered BaBi3.9RE0.1Ti4O15 (RE = La, Pr, Nd, and Sm) Aurivillius compounds. Sci Rep. 2022 Oct 3;12(1):16508.

24. Snedden A, Blake SM, Lightfoot P. Oxide ion conductivity in Ga-doped Aurivillius phases—a reappraisal. Solid State Ion. 2003 Jan 1;156(3):439–45.

25. Keeney L, Kulkarni S, Deepak N, Schmidt M, Petkov N, Zhang PF, et al. Room temperature ferroelectric and magnetic investigations and detailed phase analysis of Aurivillius phase Bi5Ti3Fe0.7Co0.3O15 thin films. J Appl Phys. 2012 Sep 4;112(5):052010.

26. Faraz A, Ricote J, Jimenez R, Maity T, Schmidt M, Deepak N, et al. Exploring ferroelectric and magnetic properties of Tb-substituted m = 5 layered Aurivillius phase thin films. J Appl Phys. 2018 Mar 22;123(12):124101.

27. Huang F, Lu X, Xu T, Liu Y, Su W, Jin Y, et al. Multiferroic properties of Co and Nd co-substituted Bi5Ti3FeO15 thin films. Thin Solid Films. 2012 Aug 31;520(21):6489–92.

28. Park BH, Kang BS, Bu SD, Noh TW, Lee J, Jo W. Lanthanum-substituted bismuth titanate for use in non-volatile memories. Nature. 1999 Oct 1;401(6754):682–4.

29. Momma K, Izumi F. ıt VESTA3 for three-dimensional visualization of crystal, volumetric and morphology data. J Appl Crystallogr. 2011 Dec;44(6):1272–6.

30. GARCÍA-GUADERRAMA M, FUENTES-MONTERO L, RODRIGUEZ A, FUENTES L. STRUCTURAL CHARACTERIZATION OF Bi6Ti3Fe2O18 OBTAINED BY MOLTEN SALT SYNTHESIS. Integr Ferroelectr. 2006 Nov 1;83(1):41–7.

31. Krzhizhanovskaya M, Filatov S, Gusarov V, Paufler P, Bubnova R, Morozov M, et al. Aurivillius Phases in the Bi4Ti3O12/BiFeO3 System: Thermal Behaviour and Crystal Structure. Z Für Anorg Allg Chem. 2005 Jul 1;631(9):1603–8.

32. Goodenough JB. JAHN-TELLER PHENOMENA IN SOLIDS. Annu Rev Mater Sci. 1998 Aug 1;28(1):1–27.

33. Zurbuchen MA, Tian W, Pan XQ, Fong D, Streiffer SK, Hawley ME, et al. Morphology, structure, and nucleation of out-of-phase boundaries (OPBs) in epitaxial films of layered oxides. J Mater Res. 2007 Jun 1;22(6):1439–71.

34. Keeney L, Saghi Z, O'Sullivan M, Alaria J, Schmidt M, Colfer L. Persistence of Ferroelectricity Close to Unit-Cell Thickness in Structurally Disordered Aurivillius Phases. Chem Mater. 2020 Dec 22;32(24):10511–23.

35. Colfer L, Keeney L, Schmidt M. Probing Ferroelectric Behavior in Sub-10 nm Bismuth-Rich Aurivillius Films by Piezoresponse Force Microscopy. Microsc Microanal. 2021/12/01 ed. 2022;28(4):1396–406.

36. Armstrong RA, Newnham RE. Bismuth titanate solid solutions. Mater Res Bull. 1972 Oct 1;7(10):1025–34.

37. Zheleva T, Jagannadham K, Narayan J. Epitaxial growth in large-lattice-mismatch systems. J Appl Phys. 1994 Jan 15;75(2):860–71.

38. Li Y, Bian M, Zhang N, Bai W, Yang J, Zhang Y, et al. Mn-doping composition dependence of the structures, electrical and magnetic properties, and domain structure/switching of Aurivillius Bi5Ti3FeO15 films. Ceram Int. 2019 May 1;45(7, Part A):8634–9.

39. Holder CF, Schaak RE. Tutorial on Powder X-ray Diffraction for Characterizing Nanoscale Materials. ACS Nano. 2019 Jul 23;13(7):7359–65.

40. Lomanova NA, Morozov MI, Ugolkov VL, Gusarov VV. Properties of aurivillius phases in the Bi4Ti3O12-BiFeO3 system. Inorg Mater. 2006 Feb 1;42(2):189–95.

41. Hervoches CH, Snedden A, Riggs R, Kilcoyne SH, Manuel P, Lightfoot P. Structural Behavior of the Four-Layer Aurivillius-Phase Ferroelectrics SrBi4Ti4O15 and Bi5Ti3FeO15. J Solid State Chem. 2002 Mar 1;164(2):280–91.

42. Ismunandar, Kamiyama T, Hoshikawa A, Zhou Q, Kennedy BJ, Kubota Y, et al. Structural studies of five layer Aurivillius oxides: A2Bi4Ti5O18 (A=Ca, Sr, Ba and Pb). J Solid State Chem. 2004 Nov 1;177(11):4188–96.

43. Zurbuchen MA, Sherman VO, Tagantsev AK, Schubert J, Hawley ME, Fong DD, et al. Synthesis, structure, and electrical behavior of Sr4Bi4Ti7O24. J Appl Phys. 2010 Jan 25;107(2):024106.

44. Silva F, Noor-A-Alam M, Nolan M, Keeney L. Predictions of Most Stable Cation Distributions Within Layered Multiferroic Bi6TixFeyMnzO18 Systems [Internet]. International Symposium on Applied Ferroelectrics-Piezoresponse Force Microscopy-European Conference on Applications of Polar Dielectrics; 2022; Tours, France. Available from: https://epapers.org/isaf2022/ESR/paper_details.php?PHPSESSID=r3pg63l4q8osh930esr7udlqv5&paper_id=2410

45. Mizusaki J, Mori N, Takai H, Yonemura Y, Minamiue H, Tagawa H, et al. Oxygen nonstoichiometry and defect equilibrium in the perovskite-type oxides La1−xSrxMnO3+d. Solid State Ion. 2000 Apr 1;129(1):163–77.

46. Flores-Lasluisa JX, Huerta F, Cazorla-Amorós D, Morallón E. Manganese oxides/LaMnO3 perovskite materials and their application in the oxygen reduction reaction. Energy. 2022 May 15;247:123456.

47. Selbach SM, Tybell T, Einarsrud MA, Grande T. High-temperature semiconducting cubic phase of \textBiFe_0.7\textMn_0.3\textO_3+\ensuremath\delta. Phys Rev B. 2009 Jun;79(21):214113.

48. Selbach SM, Tybell T, Einarsrud MA, Grande T. Structure and Properties of Multiferroic Oxygen Hyperstoichiometric BiFe1−xMnxO3+δ. Chem Mater. 2009 Nov 10;21(21):5176–86.

49. Bencan A, Drazic G, Ursic H, Makarovic M, Komelj M, Rojac T. Domain-wall pinning and defect ordering in BiFeO3 probed on the atomic and nanoscale. Nat Commun. 2020 Apr 9;11(1):1762.

50. Qi X, Dho J, Tomov R, Blamire MG, MacManus-Driscoll JL. Greatly reduced leakage current and conduction mechanism in aliovalent-ion-doped BiFeO3. Appl Phys Lett. 2005 Jan 31;86(6):062903.

51. Rajagopalan R, Chen B, Zhang Z, Wu XL, Du Y, Huang Y, et al. Improved Reversibility of Fe3+/Fe4+ Redox Couple in Sodium Super Ion Conductor Type Na3Fe2(PO4)3 for Sodium-Ion Batteries. Adv Mater. 2017 Mar 1;29(12):1605694.

52. Palizdar M, Comyn TP, Ward MB, Brown AP, Harrington JP, Kulkarni S, et al. Crystallographic and magnetic identification of secondary phase in orientated Bi5Fe0.5Co0.5Ti3O15 ceramics. J Appl Phys. 2012 Oct 8;112(7):073919.

53. Deepak N, Carolan P, Keeney L, Pemble ME, Whatmore RW. Tunable nanoscale structural disorder in Aurivillius phase, n = 3 Bi4Ti3O12 thin films and their role in the transformation to n = 4, Bi5Ti3FeO15 phase. J Mater Chem C. 2015;3(22):5727–32.

54. Lynette Keeney, Louise Colfer, Debismita Dutta, Michael Schmidt, Guannan Wei. What lies beneath? Investigations of atomic force microscopy-based nano-machining to reveal sub-surface ferroelectric domain configurations in ultrathin films. Microstructures. 2023;3(4):2023041.

55. Trolier-McKinstry S. Crystal Chemistry of Piezoelectric Materials. In: Safari A, Akdoğan EK, editors. Piezoelectric and Acoustic Materials for Transducer Applications [Internet]. Boston, MA: Springer US; 2008. p. 39–56. Available from: https://doi.org/10.1007/978-0-387-76540-2_3

56. Scott JF. Ferroelectrics go bananas. J Phys Condens Matter. 2007 Dec 13;20(2):021001.

57. Song D, Yang J, Yang B, Chen L, Wang F, Zhu X. Evolution of structure and ferroelectricity in Aurivillius Bi4Bin−3Fen−3Ti3O3n+3 thin films. J Mater Chem C. 2018;6(32):8618–27.

58. Goodenough JB. Theory of the Role of Covalence in the Perovskite-Type Manganites $[\mathrm{La}, M(\mathrm{II})]\mathrm{Mn}{\mathrm{O}}_{3}$. Phys Rev. 1955 Oct 15;100(2):564–73.

59. J B Goodenough. Electronic and ionic transport properties and other physical aspects of perovskites. Rep Prog Phys. 2004 Sep 22;67(11):1915.

60. Martin LW, Chu YH, Ramesh R. Advances in the growth and characterization of magnetic, ferroelectric, and multiferroic oxide thin films. Mater Sci Eng R Rep. 2010 May 20;68(4):89–133.